Effects of narrowband transport on near-field and far-field thermophotonic conversion

Sean McSherry, a Tobias Burger, a Andrej Lenerta,*

^aUniversity of Michigan, Department of Chemical Engineering, 2800 Plymouth Rd., Ann Arbor, MI, USA,

48109

Abstract

Thermodynamic limits suggest that near-monochromatic transmission of radiation is beneficial for photonmediated conversion of heat to electricity. However, determining the optimal bandwidth in the presence of parasitic heat losses is more complicated. Here, we study the effects of transmission bandwidth on the performance of far-field and near-field thermophotovoltaic (TPV) and thermophotonic (TPX) converters. Our analysis shows that the optimal bandwidth depends on the type of converter. For far-field TPVs with realistic heat losses, narrowband transport is typically detrimental to the efficiency because the converter becomes more susceptible to parasitic loss. However, narrowband transport boosts efficiencies in near-field enhanced and electroluminescent (TPX) converters. Enhancements in useful energy flux and efficiency in TPX conversion with respect to TPVs, with the same thermal-excitation energy barrier, is attributed to the larger photon density of states available with increasing bandgap. This study suggests that near-field TPX converters with a large applied bias have the largest ratio of useful energy flux to parasitic loss. This effect may allow near-field TPX converters to mitigate the effects of parasitic heat loss better than others. Leveraging this mechanism for actual improvement is contingent on large near-field enhancements improving photon extraction.

Keywords: Thermophotovoltaic, thermophotonic, near-field

*Andrej Lenert, E-mail: alenert@umich.edu

1. Introduction

Thermophotonic converters are solid-state converters where photon-mediated transport of

energy carriers across a potential energy barrier is driven by a temperature difference between

the hot source and the cold receiver. An example of a thermophotonic converter, with no

electrical bias applied to the hot-side, is a thermophotovoltaic converter (TPV). Useful

transport in TPVs is mediated by thermal radiation of photons with energies above the

electronic bandgap of the cold cell. The cell most efficiently converts radiation with energies

in a narrow range above the bandgap, as thermalization losses are minimized. In theory, ideal

TPVs may achieve Carnot efficiency in the limit of monochromatic transmission between the

emitter and cell (in the absence of non-radiative recombination). 1,2 It is therefore expected that

approaching monochromatic transmission in practice, via spectral control of radiative transport

between the emitter and cell, can lead to improvements in converter efficiency. Here, we

1

investigate the validity of this argument in the context of far-field converters and emerging strategies for enhancing above-bandgap transport using *near-field geometries* and *electroluminescence*.

State-of-the-art TPV converters operate with efficiencies that are far below their thermodynamic limits.^{3–7} A large contributor to this efficiency gap is the relatively low above-bandgap energy flux of emitted radiation, limited by the fraction of far-field black body radiation above the bandgap of the cell.⁸ As a result, TPV converters are susceptible to parasitic heat losses stemming from radiative heat transfer to the cell at energies below the bandgap and to the surroundings. These losses have an important role in TPV system design.^{9,10} One strategy for enhancing the energy flux in TPVs is to decrease the separation distance between the emitter and cell.^{11–25} Radiative transport between materials separated by distances less than the thermal wavelength (i.e., near-field) is characterized by (super-Planckian) high fluxes.^{25–32} While a near-field geometry can enhance above-bandgap flux without increasing emitter temperature, it often also leads to enhanced transport at energies below the bandgap (e.g., via phonon polariton modes).^{15,21,22} Under these circumstances, operation in the near-field may result in decreased TPV efficiency with respect to the far-field because of enhanced parasitic, sub-bandgap transport.^{15,22}

This work also considers a complementary strategy that aims to specifically enhance transport at energies above the bandgap without contributing to parasitic, sub-bandgap absorption mechanisms: a near-field converter that utilizes a forward-biased diode as the hot emitter. TPX energy conversion in the near-field was previously described in a patent for a power generation/cooling device consisting of an emitter and a cell separated by a sub-micron vacuum gap, where thermal emission is supplemented by electroluminescent photon emission.³³ Recently, the heat pump^{34,35} and refrigeration^{36–39} potential of this concept were further explored by analyzing transport in the near-field driven by a chemical potential

difference. However, the consequences of luminescent and near-field enhancement on the optimal transmission bandwidth in thermophotonic converters has not been studied in detail.

Here, a simplified, yet general, framework is developed to model transport and energy conversion in TPV and TPX converters and explore the effects of near-field enhancement, applied bias, transmission bandwidth, and electronic bandgap on the magnitude of above-bandgap transport. Further, we identify the existence of optimal bandwidths in these converters and develop analytical relationships to describe the enhancement of the useful energy flux. The results of this study suggest how to maximize the amount of above-bandgap transport relative to parasitic losses and, ultimately, achieve high efficiencies at relatively low operating temperatures in TPX systems. Lastly, the model is tested computationally using thermophotonic converters comprised of InAs, InGaAs, and GaAs.

2. Model Formulation

The model physical system considered here is composed of a hot emitter diode and a cold PV cell (with the same electronic bandgap, E_g) in a parallel-plate configuration with separation distances ranging from the far-field (ff) to the near-field (nf) regime (Fig. 1). To analyze the performance of the power generation system, we combine a detailed balance analysis with a radiative transport model that accounts for parasitic heat transfer and near-field enhancements as described below. Input heat (Q_h) creates a temperature differential, driving net energy flux (E_{hc}) from the emitter to the cell. Absorption of radiation generates photoexcited concentrations of electrons and holes in the cell, whose quasi-Fermi levels split, giving rise to a photon chemical potential (μ_c). Power is generated at the cell (P_{out}) by extracting current at μ_c . A portion of the output electrical power is recycled back to the emitter as input power (P_{in}) and used to establish separation between the quasi-Fermi levels of the emitter (μ_h). Recycling of generated power distinguishes a TPX system from a conventional TPV system (which has no

applied bias on the emitter). Net power generation in a TPX requires that the output power, P_{out} , be greater than the input power, P_{in} . Waste heat (Q_c) from thermalization of excited charge carriers and parasitic sub-bandgap heat transfer between the emitter and the cell (maintained at 300 K) is rejected to the environment (at 300 K). The hot emitter also parasitically loses heat (Q_{loss}) to the environment via far-field thermal radiation.

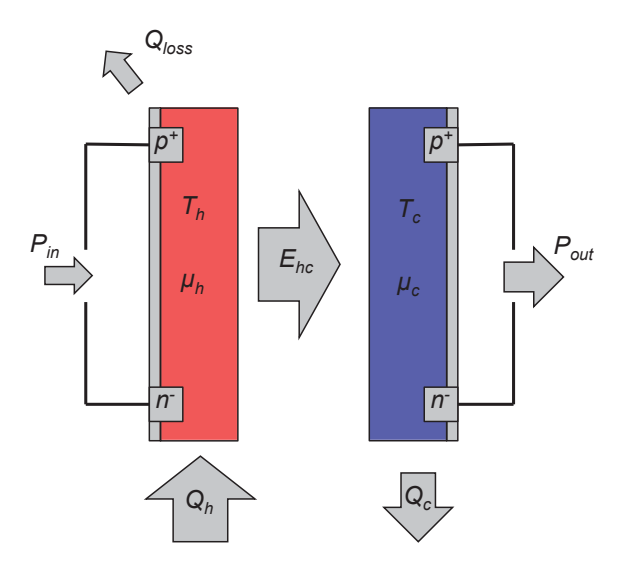


Figure 1. Schematic of a TPX power converter consisting of a hot emitter diode (at T_h) and a cold PV cell (at T_c) in a parallel-plate configuration. Input power (P_{in}) is supplied to the emitter through an electrical bias to establish a separation between the quasi-Fermi levels of the emitter (μ_h), while the input heat (Q_h) is used to create a temperature difference and drive a net energy flux (E_{hc}) between the emitter and the cell. Output power (P_{out}) is generated at the cell by extracting current at μ_c , while waste heat (Q_c) is rejected to the environment. A portion of P_{out} is recycled back to the emitter, hence supplying P_{in} . The hot emitter also loses heat (Q_{loss}) to the environment (at 300 K) via far-field thermal radiation.

Separation between the quasi-Fermi levels (μ) in a semiconductor modifies the photon occupation probability as described by Planck's generalized law,⁴⁰

$$\Theta(\omega, T, \mu) = \frac{\hbar \omega}{\exp(\frac{\hbar \omega - \mu}{kT}) - 1}$$
 (1)

where Θ is the average photon energy, T is the temperature, μ is the quasi-Fermi level splitting (or photon chemical potential), k is the Boltzmann constant, and \hbar is the reduced Planck's constant. The quasi-Fermi level splitting is non-zero only for photon energies ($\hbar\omega$) above E_g ,

corresponding to interband electronic transitions. Below the bandgap, the energy flux is assumed to be independent of the chemical potential since the flux does not correspond to photoexcited carriers. The chemical potential splitting in this study is restricted to $\mu \leq (E_g - 3kT)$, to remain in the spontaneous emission regime where Eq. 1 is valid. Further, as in Refs. 36,41 , it is assumed that the energy transport between the emitter and the cell is dominated by the exchange between their respective depletion regions; i.e., the doped regions of the diodes are assumed to be small and are, thus, neglected.

For above-bandgap modes, the net energy flux between the hot emitter (h) and the cold cell (c) is given by:

$$E_{hc}(\omega \ge \omega_g) = \int_{\omega_g}^{\infty} [\Theta_h(\omega, T_h, \mu_h) - \Theta_c(\omega, T_c, \mu_c)] \Phi(\omega) d\omega$$
 (2)

Similarly, the net photon flux is given by:

$$F_{hc}(\omega \ge \omega_g) = \int_{\omega_g}^{\infty} \frac{[\Theta_h(\omega, T_h, \mu_h) - \Theta_c(\omega, T_c, \mu_c)]}{\hbar \omega} \Phi(\omega) d\omega$$
 (3)

where ω_g is the angular frequency corresponding to the electronic bandgap, and Φ is the flux spectrum.

In general, the flux spectrum depends on the permittivity and specific geometry of the participating layers. The standard dyadic Green's function technique can be used to compute the electromagnetic flux from the thermally-driven current fluctuations and to obtain an expression for the flux spectrum, $\Phi(\omega)$. ^{25,29,42} In the first section of this work, however, we model the flux spectrum *approximately* such that behavior of converters can be easily computed and interpreted across a range of design parameters such as near-field enhancement, electronic bandgap, and transmission bandwidth. This simplified model is later compared to a rigorous calculation using Multilayer Electromagnetic Solver for Heat Transfer (MESH), a simulation tool based on fluctuation electrodynamics developed to solve near- and far-field heat transfer in multilayer structures. ⁴³

In the simplified model, a grey near-field enhancement approximation is applied, which assumes the near-field photon density of states is a scaled version of the far-field photon density of states, $D(\omega)$:

$$\Phi(\omega_g \le \omega < \omega_g + \Delta\omega) = f_{nf}\left(\frac{c}{4}\right)D(\omega) = f_{nf}\frac{\omega^2}{4\pi^2c^2}$$
 (4)

where f_{nf} is the near-field enhancement factor, $\Delta \omega$ is the above-bandgap transmission bandwidth between the emitter and the cell, and c is the speed of light in vacuum.

This approximation comes from the well-known n^2 limit for near-field enhancement between two weakly-absorbing materials, where n is the real part of the refractive index. 27,28,44 The approximation is valid if the imaginary part is much smaller than n. Furthermore, $\varepsilon(\omega)$ should not be a strong function of ω over the spectral width of the contributing energy flux; this should hold when the occupation probability is peaked near the bandgap (i.e., when $\hbar\omega_g - \mu > 3kT_h$) and/or the transmission bandwidth is narrow. This is a reasonable approximation of above-bandgap properties for bulk semiconductors of interest for TPV and TPX applications, such as InAs and InGaAs (see Appendix A for a comparison of the approximation to a rigorous simulation using MESH). For far-field radiative heat transfer ($f_{nf} = 1$), on the other hand, the model simply describes transport between two black bodies above the bandgap.

Using these abstractions, the spectral energy flux of far-field and near-field TPV and near-field TPX converters are described (Fig. 2). Near-field enhancement factors range significantly for simulated near-field TPVs reported in literature; $^{15,21-23}$ hence, we define f_{nf} as a variable parameter.

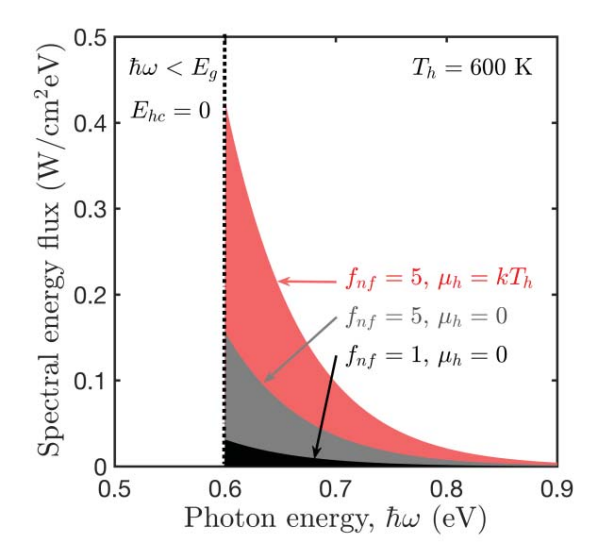


Figure 2. Spectral energy flux from a far-field, black body (BB) emitter (black), a near-field emitter (gray), and a near-field emitter with a small applied bias (red) at an emitter temperature of $T_h = 600$ K. The near-field enhancement factor ($f_{nf} = 5$), applied bias ($\mu_h = kT_h$), and bandgap ($E_g = 0.6$ eV) were chosen arbitrarily for illustration of their effect on the spectral energy flux.

To find the net output electrical power, the power input to the system to drive active emission (P_{in}) is subtracted from the output power of the cell (P_{out}) , where:

$$P_{in} = \mu_h \cdot F_{hc} \tag{5}$$

$$P_{out} = \mu_c \cdot F_{hc} \tag{6}$$

The efficiency of the system, η , is evaluated from the net power output using the standard heatengine form:

$$\eta = \frac{P_{out} - P_{in}}{Q_h} \tag{7}$$

where Q_h is the total heat input into the emitter:

$$Q_h = E_{hc} - P_{in} + Q_{loss} \tag{8}$$

 Q_h is obtained by taking an energy balance around the emitter. Additionally, the model considers intrinsic heat loss to the environment dominated by radiation: $Q_{loss} = \varepsilon_{sys}\sigma(T_h^4 - T_C^4)$, where σ is the Stefan-Boltzmann constant. The magnitude of heat loss depends on the type of heat source and the geometry of the system. To reflect the best-reported⁵⁻⁷ TPVs and scaled-

up solar TPV systems,^{9,45} the effective emittance (ε_{sys}) is set to 0.05 (excluding the idealized case). For the purposes of our study, the effects of non-radiative recombination and subbandgap flux may be captured by increasing the Q_{loss} term. We do not explicitly model the effects of non-radiative recombination and sub-bandgap flux because the focus of the analysis is on effects of variable transmission bandwidth, not on the absolute efficiency of the system. The non-radiative rate depends only on the temperature and the applied bias and is independent of the near-field enhancement and the transmission bandwidth.^{21,46–49}

3. Effects of narrowband transmission

The following analysis describes the impact of parasitic heat losses to the environment on TPV and TPX converter performance and optimal transmission bandwidth (based on the simplified model described above). Three different converters are considered:

TPX a TPX converter with a bandgap $E_{gl} = 1$ eV and an applied bias of $\mu_h = E_{gl} - 4kT_h$

 TPV_{leV} a TPV converter with a large bandgap $E_{gl} = 1$ eV (relative to kT_h)

 TPV_{4kT} a TPV converter with a bandgap $E_{g2} = 4kT_h$, which is more comparable to the thermal energy.

Each converter operates with a hot emitter at $T_h = 600$ K, and a cold cell at $T_c = 300$ K. The calculated conversion efficiency as a function of transmission bandwidth for ideal converters operating in the far-field with no parasitic loss (Fig. 3a) is compared to converters with parasitic heat loss to the environment ($\varepsilon_{sys} = 0.05$) in the far-field (Fig. 3b) and near-field (Fig. 3c) regimes.

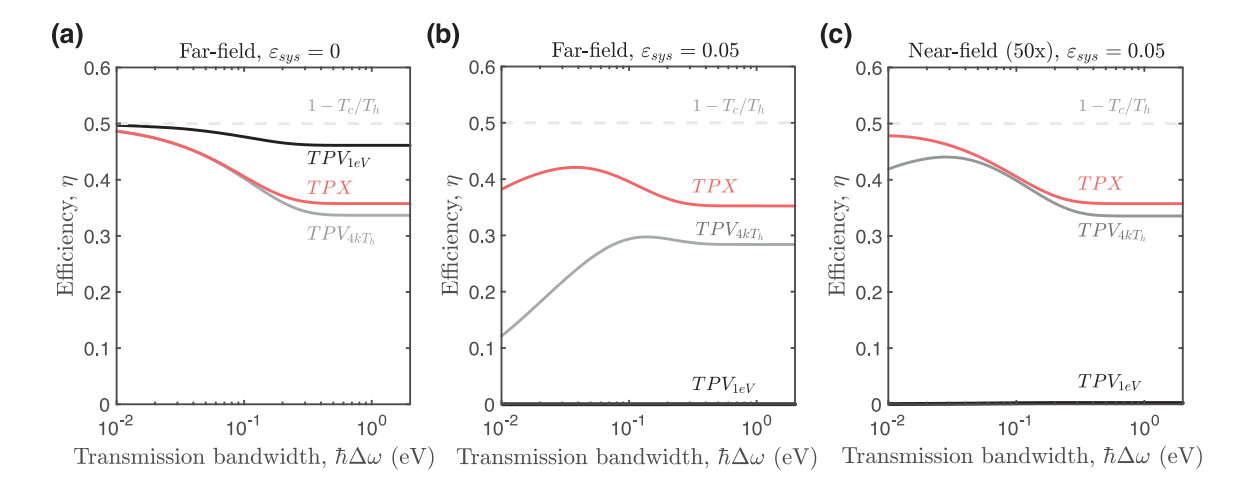


Figure 3. Efficiency as a function of transmission bandwidth for the following converters: (a) far-field, no parasitic heat losses ($\varepsilon_{sys} = 0$), (b) far-field, parasitic heat loss to the environment ($\varepsilon_{sys} = 0.05$), and (c) near-field ($f_{nf} = 50$), parasitic heat loss to the environment ($\varepsilon_{sys} = 0.05$). TPX with $E_{gl} = 1$ eV and $\mu_h = E_{gl} - 4kT_h$ (red), TPV_{leV} (black), and TPV_{4kT} (gray) are compared in each case. Carnot efficiency (dashed) is shown for reference. $T_h = 600$ K, $T_c = 300$ K.

In the ideal case ($\varepsilon_{sys} = 0$), each converter approaches the Carnot limit (1 – T_c/T_h) as the transmission bandwidth narrows and approaches the monochromatic limit (Fig. 3a). For large transmission bandwidths, excess energy (exceeding the bandgap) is lost to thermalization and, thus, reduces the efficiency of the converter. We verified that all converters with a near-field enhancement factor greater than 1 will also approach the Carnot limit (this is because the limit is governed by thermodynamic laws and not by transport).

In the presence of heat loss (Q_{loss}) to the environment from the 600 K hot emitter, TPV_{leV} is most severely affected by parasitic losses (Fig. 3b,c), exhibiting the lowest predicted efficiency (near-zero) at all bandwidths considered. For converters with lower bandgaps, such as TPV_{4kT} , the efficiency is more resilient to parasitic loss. However, TPV_{4kT} is also susceptible to parasitic loss as the transmission bandwidth narrows.

For far-field TPV converters in the presence of parasitic heat loss (Fig. 3b), we generally observe that as the transmission bandwidth is narrowed, the converter efficiency decreases. The competing effects of decreased energy flux (at low transmission-bandwidths) and

increasing thermalization losses (at high bandwidths) give rise to a finite, optimal bandwidth. To summarize, near-monochromatic emission/absorption does *not* translate to higher conversion efficiencies for far-field TPVs when considering reasonable parasitic losses, contrary to the idealized case which often guides intuition and component-level design. We have verified that this effect is observed even at higher emitter temperatures ($T_h = 1200 \text{ K}$) (see Appendix B).

A TPX converter with a large bandgap ($E_{gl} = 1 \text{ eV}$) and an applied bias ($\mu_h = E_{gl} - 4kT_h$) maintains high efficiency, even for small transmission bandwidths. This potentially motivates the use of low-dimensional photonic materials such as waveguides²¹ and further study of low-dimensional electronic materials,^{50,18–20,23,51} such as quantum wells for enhanced luminescence.

Near-field enhancement generally leads to improved efficiency and narrowing of the optimal bandwidth (Fig. 3c). As the near-field-enhanced energy flux overpowers the far-field parasitic loss, narrowband operation becomes optimal. The near-field TPX converter has the highest overall efficiency. However, achieving this high near-field enhancement (*i.e.*, approaching the n^2 limit) for a TPX converter with a large bandgap (e.g., 1 eV), would require a small gap to maintain the ratio of the characteristic free-space wavelength, λ_g (corresponding to the bandgap energy), to the gap size, d.

The efficiency trends discussed above (and in Fig. 3) can be explained by the relative magnitude of the useful energy flux (Fig. 4), defined here as E_{hc} — P_{in} , compared to the parasitic heat loss (Q_{loss}). The TPX maintains the highest efficiency across all bandwidths because it has the largest useful energy flux compared to the other converters, as discussed further in the following section.

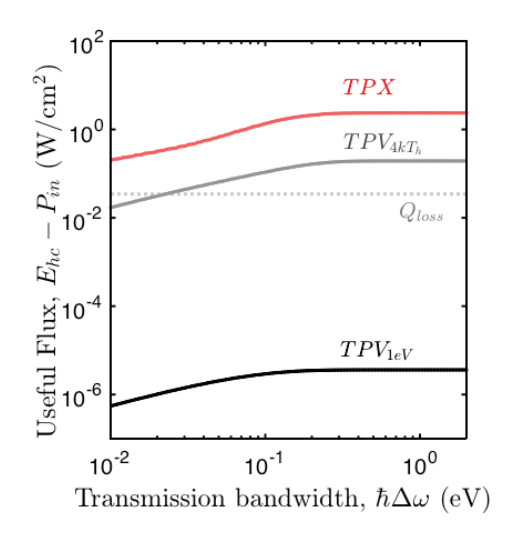


Figure 4. Useful energy flux $(E_{hc} - P_{in})$ for far-field converters with heat loss to the environment $(\varepsilon_{sys} = 0.05)$, corresponding to Fig. 3b. The following converters are compared: TPX with $E_{gl} = 1$ eV and $\mu_h = E_{gl} - 4kT_h$ (red), TPV_{leV} (black), and TPV_{4kT} (gray). Q_{loss} (dashed) is shown for reference.

4. Analytical analysis of the useful energy flux across converters

Here, we aim to rationalize the difference in useful energy flux between the three converters $(TPX, TPV_{IeV}, \text{ and } TPV_{4kT})$, which is important to understanding their efficiencies and optimal transmission bandwidths. It is assumed that the spectral energy flux is sharply peaked near the bandgap frequency (Boltzmann approximation), indicating that the resulting integral from equations 2-4 are dominated by the leading term. It is also assumed that the net flux is dominated by the emitter. Under these conditions,

$$E_{hc} \approx \hbar \omega_g exp\left(-\frac{\Delta_g}{kT_h}\right) \Phi(\omega_g) \left(\frac{kT_h}{\hbar}\right)$$
 (9a)

$$P_{in} \approx \mu_h exp\left(-\frac{\Delta_g}{kT_h}\right) \Phi(\omega_g) \left(\frac{kT_h}{\hbar}\right)$$
 (9b)

where Δ_g is the thermal energy barrier at the emitter ($\Delta_g = \hbar \omega_g - \mu_h$). By subtracting the power input from the energy flux, an expression for the useful energy flux is obtained.

$$E_{hc} - P_{in} = \Delta_g \exp\left(-\frac{\Delta_g}{kT_h}\right) \Phi(\omega_g) \left(\frac{kT_h}{\hbar}\right)$$
 (10)

Assuming the near-field enhancement is equal for both converters, the useful energy flux ratio

of TPV_{leV} relative to TPV_{4kT} (or total energy flux ratio in this case since $\mu_h = 0$, $P_{in} = 0$ for both) is given by

$$\frac{(E_{hc} - P_{in})_{TPV}}{(E_{hc} - P_{in})_{TPV}} = \left(\frac{E_{g,TPV1eV}}{E_{g,TPV4kT}}\right)^3 exp\left(-\frac{E_{g,TPV1eV} - E_{g,TPV4kT}}{kT_h}\right)$$
(11)

where $\hbar\omega_g$ is set to the appropriate E_g for the relevant material. From this expression, the energy flux for TPV_{leV} is expected to be ~10⁵ times lower than that for TPV_{4kT} , which is consistent with results shown in Fig. 4.

Similarly, we compare the useful energy flux of the TPX converter to that of TPV_{4kT} . Despite the wide bandgap of the TPX converter, the applied bias decreases the energy barrier such that it is equal to the bandgap of TPV_{4kT} ($\Delta_g = E_{g2} = E_{g1} - \mu_h = 4kT_h$). Thus, both converters have the same probability of occupying states above the bandgap. The ratio of the useful energy flux of the TPX relative to that of the TPV_{4kT} , is simply the square of the ratio of their photon density of states at their respective bandgap frequencies,

$$\frac{(E_{hc} - P_{in})_{TPX}}{(E_{hc} - P_{in})_{TPY}} = \left(\frac{D(\omega_{g,TPX})}{D(\omega_{g,TPY})}\right)^2 = \left(\frac{E_{g,TPX}}{E_{g,TPY}}\right)^2$$
(12)

which is ~25 in this case, in agreement with Fig. 4. The power enhancement, and ultimately the efficiency of the TPX converter, is therefore attributed to the fact that the photon density of states increases with photon energy, and is significantly larger at $E_{gl} = 1$ eV than at $E_{g2} = 4$ kT_h = 0.207 eV.

5. Rigorous analysis of useful energy flux in thermophotonic converters

Thus far, we have applied several key assumptions in our formulation and analysis to describe the efficiency and useful energy flux of converters. Here, we employ MESH to test the validity of our assumptions for near-field transport. MESH was utilized to compute the near-field energy and photon flux for two TPX converters and a reference TPV converter, and to assess the E_g^2 scaling of the useful energy flux (Eq. 12). The defining characteristics of each converter are presented in Table 1.

Table 1. Converter parameters for the rigorous analysis of useful energy flux.

Converter	E_g [eV]	μ_h [eV]	$\Delta_g = E_g - \mu_h \text{ [eV]}$
$TPV_{0.354eV}$	0.354	0	0.354
$TPX_{0.75eV}$	0.750	0.396	0.354
$TPX_{1.424eV}$	1.424	1.070	0.354

The bandgaps of the converters ($TPV_{0.354eV}$, $TPX_{0.75eV}$, and $TPX_{1.424eV}$) were chosen to reflect those of InAs, In_{0.53}Ga_{0.47}As (hereafter InGaAs), and GaAs, a class of semiconductors commonly used in TPVs. The applied bias for each TPX converter was set to achieve an energy barrier (Δ_g) equivalent to that of the reference TPV converter. The real and imaginary components of the refractive index were set to the same constant values (n = 3.3, k = 0.1) for each converter to mimic the behavior of weakly absorbing semiconductors. The above-bandgap energy flux was computed for $T_h = 600 \text{K}$ and $T_c = 300 \text{K}$. The power enhancement relative to the reference TPV was simulated for each TPX converter as a function of the gap size normalized by the bandgap wavelength (Fig. 5a). The simulated results agree well with the $E_{\rm g}^2$ scaling in the extreme and mid near-field for both TPX – TPV comparisons. Deviations from the model occur most likely because of error associated with the assumptions made in Eq. 9. For example, it was previously assumed that energy flux is dominated by emission at or near the band-edge. However, it is apparent that useful energy transport occurs over transmission bandwidths ($\hbar\Delta\omega$) exceeding 0.5 eV in each case (Fig. 5b). Further, the rigorous simulation considers radiative emission from the cold cell ($T_c = 300$ K) to the hot emitter ($T_h = 600$ K), whereas this contribution was assumed negligible compared to emission from the emitter in the simplified analysis.

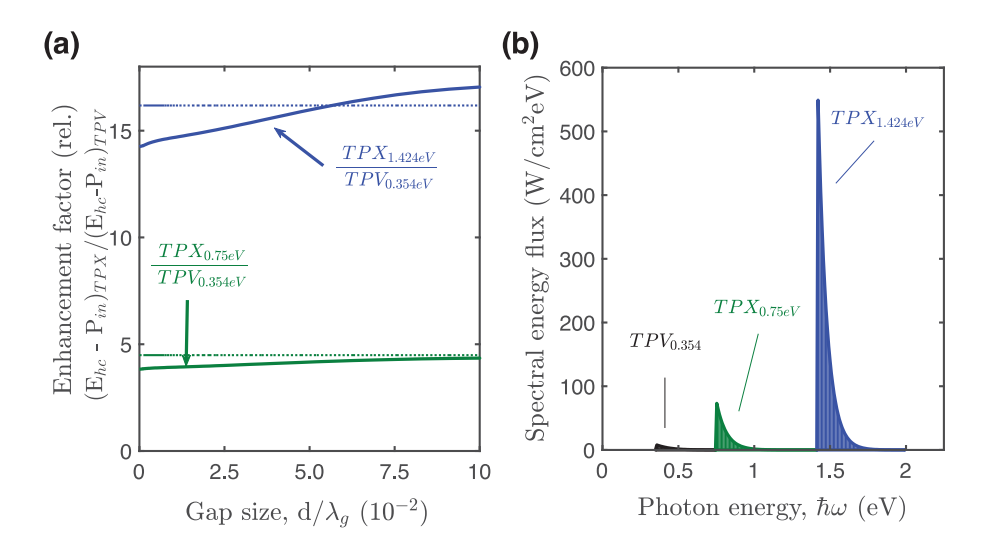


Figure 5. (a) Simulated energy-flux enhancement factor for $TPX_{1.424\text{eV}}$ relative to $TPV_{0.354\text{eV}}$ (green, solid) and $TPX_{0.75\text{eV}}$ relative to $TPV_{0.354\text{eV}}$ (blue, solid) compared to the scaling relationship presented in Eq. 12 (dotted). (b) Above-bandgap spectral energy flux for $TPV_{0.354\text{eV}}$ (black), $TPX_{0.75\text{eV}}$ (green), and $TPX_{1.424\text{eV}}$ (blue). All converters have the same Δ_g : equal probability of occupying states above their respective bandgaps.

In reality, semiconductors with different bandgaps have variable optical properties and will not behave exactly like weakly absorbing semiconductors. Therefore, the near-field enhancement factor, described by the n^2 limit, will differ for each converter. This effect is demonstrated by repeating the previous simulations with the realistic, frequency-dependent optical properties of InAs, InGaAs, and GaAs (from literature^{52–54}) for $TPV_{0.354eV}$, $TPX_{0.75eV}$, and $TPX_{1.424eV}$, respectively. The relative TPX flux enhancement is shown with respect to the normalized gap (Fig. 6). Our scaling relationship may overestimate the simulated results for the relative flux enhancement in the GaAs TPX converter (relative to InAs) due to several factors: i) the mismatch in material-specific optical properties, ii) non-monochromatic energy flux, and iii) cold cell emission. The relative flux enhancement in the InGaAs TPX converter agrees with the model, suggesting that these competing errors may negate each other.

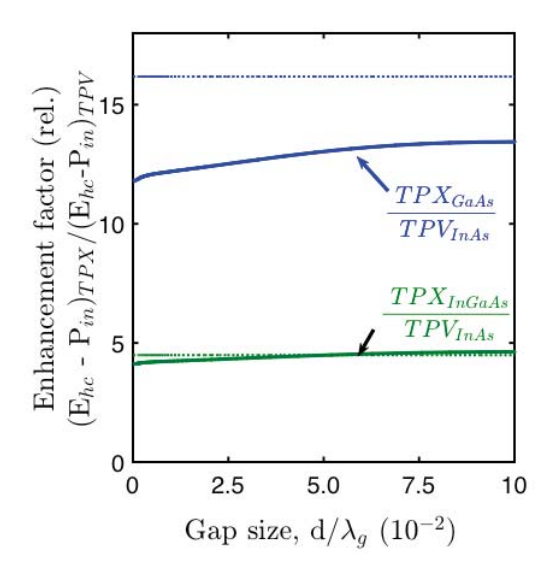


Figure 6. Simulated power enhancement factor for $TPX_{GaAs} - TPV_{InAs}$ (red, solid) and $TPX_{InGaAs} - TPV_{InAs}$ (black, solid) compared to the scaling relationship presented in Eq. 12 (dashed lines).

This rigorous analysis demonstrates that wide bandgap materials, such as GaAs, can provide high useful energy fluxes at low temperatures given sufficient bias (μ_h). This result reflects ongoing efforts that aim to establish thermophotonic cooling in high-power LEDs by focusing on wider bandgap materials (i.e., GaAs-AlGaAs heterostructures). 51,55 Currently, however, LEDs with wall-plug efficiencies exceeding 100% have only been experimentally demonstrated with narrow bandgap materials (i.e., InGaAsSb) at low biases (sub-thermal: $\mu_h < kT_h$); 56,57 although operating in this regime would still improve the power conversion efficiency, the enhancement in useful flux would be low since it is proportional to $exp(\mu_h/kT_h)$. Other efforts in thermophotonic cooling include operation at elevated temperatures (400-600 K)55, and improving light extraction via near-field geometries. Furthermore, as in near-field TPV, the practicality of nanoscale vacuum gaps, spatial distribution of photocurrent generation and thermal management issues represent practical concerns for near-field TPX.¹⁷

5 Conclusions

A simple, yet general, model was developed to describe transport and energy conversion in a class of thermophotonic converters as a function of transmission bandwidth, temperature, bandgap, applied bias, and near-field enhancement. Our analysis shows that the optimal transport bandwidth depends on the type of thermophotonic converter and on the presence of parasitic heat losses. We confirmed that all idealized converters approach the Carnot limit as the bandwidth narrows. For far-field TPVs with realistic heat losses, narrowband transport is detrimental to the converter efficiency because the system becomes more susceptible to parasitic loss (i.e., broadband above-bandgap transmission is optimal). However, narrowband transport boosts efficiencies in near-field enhanced and electroluminescent (TPX) converters. Enhancements in useful energy flux and efficiency in TPX conversion with respect to TPVs, with the same thermal-excitation energy barrier, were described using an analytical expression which shows that the larger photon density of states with increasing bandgap is responsible for the enhancement. To validate this bandgap-squared scaling relationship, we compare our results to the flux for InAs, InGaAs, and GaAs converters calculated using a rigorous electromagnetic heat transfer solver. The results of this study suggest that near-field TPX converters with a large applied bias have the largest ratio of useful energy flux to parasitic losses, potentially enabling them to perform at higher efficiencies in comparison to other converters.

Appendix A: Validating the Near-field Approximation for InAs and In_{0.53}Ga_{0.47}As

The spectral energy flux from an emitter at 600 K to a receiver at 300 K was calculated with the near-field enhancement approximation and compared to the above-bandgap spectral energy flux of InAs and In_{0.53}Ga_{0.47}As (hereafter InGaAs) determined with the Multilayer Electromagnetic Solver for Heat transfer (MESH) simulation tool (Fig. 7). MESH, a program built with principles from rigorous coupled wave analysis (RWCA) and scattering-matrix formalism, inputs the frequency-dependent complex dielectric function index ($\epsilon = n^2$), and computes the flux spectrum for near-field and far-field geometries.⁴³ For the simulated results, the refractive index of InAs and InGaAs were taken from literature.⁵²⁻⁵⁴ (The spectral energy flux described by the near-field enhancement approximation for InAs ($f_{nf} = 13$) and InGaAs ($f_{nf} = 12.8$) agrees with MESH. The f_{nf} values are similar to the n^2 values for InAs and InGaAs, 12.07 and 12.3, respectively. Deviations are present due to above-bandgap absorption.

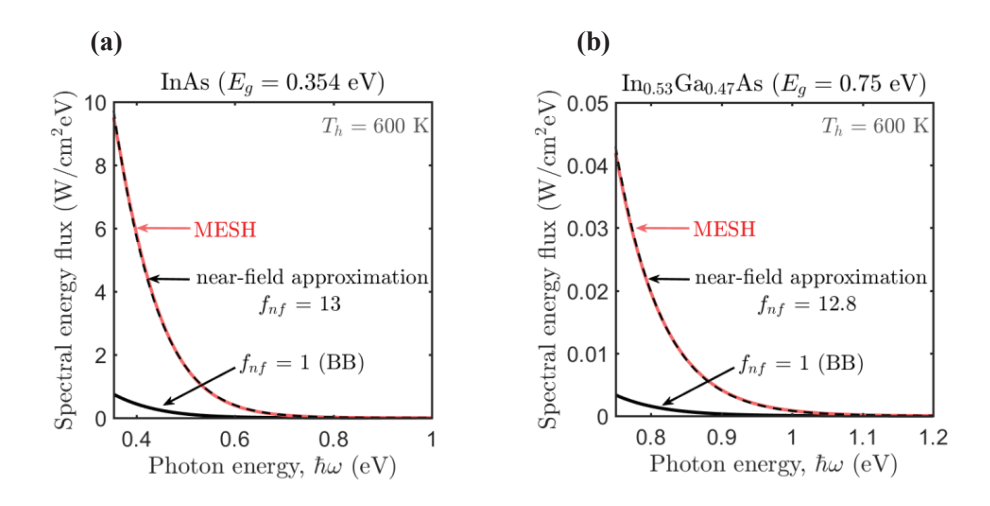


Figure 7. The spectral energy flux of (a) InAs and (b) InGaAs computed with MESH are compared to the spectral energy flux determined with the near-field approximation with near-field enhancement factors of 13 and 12.8 respectively.

Appendix B: *Efficiency of Thermophotonic Converters at* $T_h = 1200 K$

Under ideal conditions, the efficiencies of a TPX with $E_{gl} = 1$ eV and $\mu_h = E_{gl} - 4kT_h$ (TPX), a TPV with $E_{gl} = 1$ eV (TPV_{leV}), and a TPV with $E_{g2} = 4kT_h$ (TP_{V4kT}) approach the Carnot limit as the transmission bandwidth decreases (Fig 8, dashed). When parasitic losses are included (fig 8, solid), the optimal efficiency of each converter occurs at finite transmission bandwidths. In the case of a wide bandgap TPV ($TPV_{Eg=1}$), the optimal transmission bandwidth increases as the transmission bandwidth increases, defying the conventional monochromatic assumption.

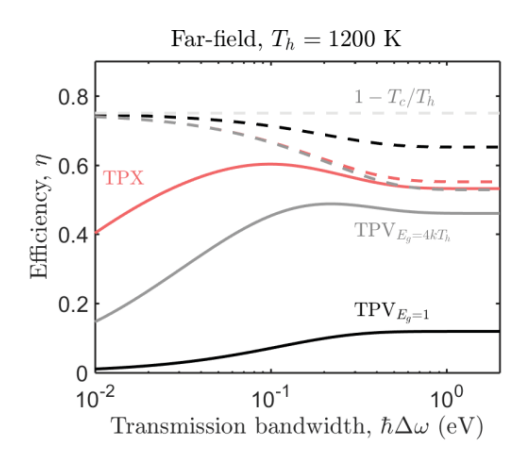


Figure 8. Efficiency of TPX (red), TPV_{4kT} (gray), and TPV_{IeV} (red) under idealistic conditions (dashed) and with parasitic losses (solid).

Acknowledgements

This material is based upon work supported by the National Science Foundation under Grant No. IIP-1820395. The authors acknowledge Luke Brechtelsbauer, David M. Bierman, Anthony Fiorino, Bai Song, Pramod Reddy and Edgar Meyhofer for their input. S.M. also acknowledges support provided by an NSF GRFP.

References

- 1. A. De Vos, *Thermodynamics of Solar Energy Conversion*, John Wiley & Sons (2008).
- 2. N.-P. Harder and P. Wurfel, "Theoretical limits of thermophotovoltaic solar energy conversion," Semicond. Sci. Technol. **18**(5), S151 (2003) [doi:10.1088/0268-1242/18/5/303].
- 3. L. M. Fraas et al., "Thermophotovoltaic system configurations and spectral control," Semicond. Sci. Technol. **18**(5), S165 (2003) [doi:10.1088/0268-1242/18/5/305].
- 4. C. J. Crowley et al., "Thermophotovoltaic Converter Performance for Radioisotope Power Systems," 2005, 601–614, AIP Publishing [doi:10.1063/1.1867178].
- 5. D. N. Woolf et al., "High-efficiency thermophotovoltaic energy conversion enabled by a metamaterial selective emitter," Optica 5(2), 213 (2018) [doi:10.1364/OPTICA.5.000213].
- 6. R. M. Swanson, "Silicon photovoltaic cells in thermophotovoltaic energy conversion," in International Electron Devices Meeting, pp. 70–73 (1978) [doi:10.1109/IEDM.1978.189354].
- 7. Y. Z. Yu et al., "High-Efficiency Multi-Cell TPV Module Fabrication and Performance," in AIP Conference Proceedings **653**(2003), pp. 335–343 (2003) [doi:10.1063/1.1539388].
- 8. T. J. Coutts, G. Guazzoni, and J. Luther, "An overview of the fifth conference on thermophotovoltaic generation of electricity," Semicond. Sci. Technol. **18**(5) (2003) [doi:10.1088/0268-1242/18/5/302].
- 9. A. Lenert et al., "A nanophotonic solar thermophotovoltaic device," Nat. Nanotechnol. **9**(2), 126–130, Nature Publishing Group (2014) [doi:10.1038/nnano.2013.286].
- 10. A. Lenert et al., "Role of spectral non-idealities in the design of solar thermophotovoltaics," Opt. Express **22**(S6), A1604 (2014) [doi:10.1364/OE.22.0A1604].
- 11. J. L. Pan, H. K. H. Choy, and J. Fonstad, "Very large radiative transfer over small distances from a black body for thermophotovoltaic applications," IEEE Trans. Electron Devices **47**(1), 241–249 (2000) [doi:10.1109/16.817591].
- 12. R. S. DiMatteo et al., "Enhanced photogeneration of carriers in a semiconductor via coupling across a nonisothermal nanoscale vacuum gap," Appl. Phys. Lett. **79**(12), 1894–1896 (2001) [doi:10.1063/1.1400762].
- 13. M. D. Whale and E. G. Cravalho, "Modeling and performance of microscale thermophotovoltaic energy conversion devices," IEEE Trans. Energy Convers. **17**(1), 130–142 (2002) [doi:10.1109/60.986450].
- M. Laroche, R. Carminati, and J. J. Greffet, "Near-field thermophotovoltaic energy conversion,"
 J. Appl. Phys. 100(6) (2006) [doi:10.1063/1.2234560].
- 15. K. Park et al., "Performance analysis of near-field thermophotovoltaic devices considering absorption distribution," J. Quant. Spectrosc. Radiat. Transf. **109**(2), 305–316 (2008) [doi:10.1016/j.jqsrt.2007.08.022].
- 16. A. Narayanaswamy and G. Chen, "Surface modes for near field thermophotovoltaics," Appl.

- Phys. Lett. **82**(20), 3544 (2003) [doi:10.1063/1.1575936].
- M. Francoeur, R. Vaillon, and M. P. Mengüç, "Thermal Impacts on the Performance of Nanoscale-Gap Thermophotovoltaic Power Generators," IEEE Trans. Energy Convers. 26(2), 686–698 (2011) [doi:10.1109/TEC.2011.2118212].
- 18. O. Ilic et al., "Overcoming the black body limit in plasmonic and graphene near-field thermophotovoltaic systems," Opt. Express **20**(S3), A366 (2012) [doi:10.1364/OE.20.00A366].
- 19. R. Messina and P. Ben-Abdallah, "Graphene-based photovoltaic cells for near-field thermal energy conversion," Sci. Rep. **3**, 1–5 (2013) [doi:10.1038/srep01383].
- 20. V. B. Svetovoy and G. Palasantzas, "Graphene-on-Silicon Near-Field Thermophotovoltaic Cell," Phys. Rev. Appl. **2**(3), 1–6 (2014) [doi:10.1103/PhysRevApplied.2.034006].
- 21. J. K. Tong et al., "Thin-film 'Thermal Well' Emitters and Absorbers for High-Efficiency Thermophotovoltaics," Sci. Rep. 5 (2015) [doi:10.1038/srep10661].
- K. Chen, P. Santhanam, and S. Fan, "Suppressing sub-bandgap phonon-polariton heat transfer in near-field thermophotovoltaic devices for waste heat recovery," Appl. Phys. Lett. 107(9) (2015) [doi:10.1063/1.4929949].
- 23. S. Molesky and Z. Jacob, "Ideal near-field thermophotovoltaic cells," Phys. Rev. B **91**(20), 205435 (2015) [doi:10.1103/PhysRevB.91.205435].
- 24. A. Fiorino et al., "Nanogap near-field thermophotovoltaics," Nat. Nanotechnol. **13**(September), 1–6, Springer US (2018) [doi:10.1038/s41565-018-0172-5].
- 25. S. Basu, Z. M. Zhang, and C. J. Fu, "Review of near-field thermal radiation and its application to energy conversion," Int. J. Energy Res. **33**(13), 1203–1232 (2009) [doi:10.1002/er.1607].
- 26. K. Joulain et al., "Surface electromagnetic waves thermally excited: Radiative heat transfer, coherence properties and Casimir forces revisited in the near field," Surf. Sci. Rep. **57**(3–4), 59–112 (2005) [doi:10.1016/j.surfrep.2004.12.002].
- 27. E. Cravalho, C. Tien, and R. P. Caren, "Effect of Small Spacings on Radiative Transfer Between Two Dielectrics," J. Heat Transfer **89**(4), 351–358 (1967) [doi:10.1115/1.3614396].
- 28. J. L. Pan, "Radiative transfer over small distances from a heated metal," 369–371 (2000).
- 29. B. Song et al., "Near-field radiative thermal transport: From theory to experiment," AIP Adv. 5(5) (2015) [doi:10.1063/1.4919048].
- 30. D. Polder and M. Van Hove, "Theory of radiative heat transfer between closely spaced bodies," Phys. Rev. B 4(10), 3303–3314 (1971) [doi:10.1103/PhysRevB.4.3303].
- 31. S. M. Rytov, Y. A. Kravtsoy, and V. I. Tatarskii, *Priniciples of statistical radiophysics (vol 3) Elements of random fields*, Springer, Berlin, Heidelberg (1989).
- 32. S. M. Rytov, *Theory of Electric Fluctuations and Thermal Radiation*, in air force cambridge research center, Bedford (1959).
- 33. R. DiMatteo, "United States Patent Application: 0090188549 Method of and apparatus for improved thermophotonic generation of electricity," 20090188549.

- 34. J. Oksanen and J. Tulkki, "Thermophotonic heat pump—a theoretical model and numerical simulations," J. Appl. Phys. **107**(9), 093106 [doi:10.1063/1.3419716].
- 35. E. Tervo, E. Bagherisereshki, and Z. Zhang, "Near-field radiative thermoelectric energy converters: a review," Front. Energy 12(1), 5–21 (2018) [doi:10.1007/s11708-017-0517-z].
- 36. K. Chen et al., "Heat-flux control and solid-state cooling by regulating chemical potential of photons in near-field electromagnetic heat transfer," Phys. Rev. B Condens. Matter Mater. Phys. **91**(13), 1–8 (2015) [doi:10.1103/PhysRevB.91.134301].
- 37. X. Liu and Z. M. Zhang, "High-performance electroluminescent refrigeration enabled by photon tunneling," Nano Energy **26**, 353–359, Elsevier (2016) [doi:10.1016/j.nanoen.2016.05.049].
- 38. K. Chen et al., "High-performance near-field electroluminescent refrigeration device consisting of a GaAs light emitting diode and a Si photovoltaic cell," J. Appl. Phys. **122**(14) (2017) [doi:10.1063/1.5007712].
- 39. C. Lin et al., "A coherent description of thermal radiative devices and its application on the near-field negative electroluminescent cooling," Energy **147**, 177–186, Elsevier Ltd (2018) [doi:10.1016/j.energy.2018.01.005].
- 40. P. Wurfel, "The chemical potential of radiation," J. Phys. C Solid State Phys. **15**(18), 3967 (1982) [doi:10.1088/0022-3719/15/18/012].
- 41. N. Harder and M. A. Green, "Thermophotonics" (2003).
- 42. W. C. Chew, Waves and fields in inhomogeneous media, IEEE Press, New York (1995).
- 43. K. Chen, B. Zhao, and S. Fan, "MESH: A free electromagnetic solver for far-field and near-field radiative heat transfer for layered periodic structures," Comput. Phys. Commun. **231**, 163–172, Elsevier B.V. (2018) [doi:10.1016/j.cpc.2018.04.032].
- 44. Z. M. Zhang, *Nano/Microscale Heat Transfer*, McGraw-Hill, New York (2007).
- 45. D. M. Bierman et al., "Enhanced photovoltaic energy conversion using thermally based spectral shaping," Nat. Energy 1(6) (2016) [doi:10.1038/nenergy.2016.68].
- 46. P. M. Fourspring et al., "Optical coatings for thermophotovoltaic spectral control," Appl. Opt. **45**(7), 1356 (2006) [doi:10.1364/AO.45.001356].
- 47. J. B. Chou et al., "Enabling ideal selective solar absorption with 2D metallic dielectric photonic crystals," Adv. Mater. **26**(47), 8041–8045 (2014) [doi:10.1002/adma.201403302].
- 48. V. Rinnerbauer et al., "Superlattice photonic crystal as broadband solar absorber for high temperature operation," Opt. Express **22**(S7), A1895 (2014) [doi:10.1364/OE.22.0A1895].
- 49. A. Kohiyama et al., "Narrowband thermal radiation from closed-end microcavities," J. Appl. Phys. **118**(13) (2015) [doi:10.1063/1.4931375].
- 50. K. R. Catchpole et al., "Thin semiconducting layers and nanostructures as active and passive emitters for...," Phys. E **14**, 91–95 (2002) [doi:10.1016/S1386-9477(02)00363-6].
- 51. O. Heikkilä, J. Oksanen, and J. Tulkki, "The challenge of unity wall plug efficiency: The effects of internal heating on the efficiency of light emitting diodes," J. Appl. Phys. **107**(3) (2010)

- [doi:10.1063/1.3285431].
- 52. E. D. Palik, Handbook of Optical Constants of Solids, Academic Press (1998).
- 53. J. R. Dixon and J. M. Ellis, "Optical properties of N-type indium arsenide in the fundamental absorption edge region," Phys. Rev. **123**(5), 1560–1566 (1961) [doi:10.1103/PhysRev.123.1560].
- 54. M. D. Sturge, "Optical absorption of gallium arsenide between 0.6 and 2.75 eV," Phys. Rev. **127**(3), 768–773 (1962) [doi:10.1103/PhysRev.127.768].
- 55. O. Heikkilä, J. Oksanen, and J. Tulkki, "Ultimate limit and temperature dependency of light-emitting diode efficiency," J. Appl. Phys. **105**(9), 093119 (2009) [doi:10.1063/1.3125514].
- 56. P. Santhanam, D. J. Gray, and R. J. Ram, "Thermoelectrically pumped light-emitting diodes operating above unity efficiency," Phys. Rev. Lett. **108**(9), 1–5 (2012) [doi:10.1103/PhysRevLett.108.097403].
- 57. P. Santhanam et al., "Room temperature thermo-electric pumping in mid-infrared light-emitting diodes," Appl. Phys. Lett. **103**(18), 183513 (2013) [doi:10.1063/1.4828566].

Caption List:

Figure 1. Schematic of a TPX power converter consisting of a hot emitter diode (at T_h) and a cold PV cell (at T_c) in a parallel-plate configuration. Input power (P_{in}) is supplied to the emitter through an electrical bias to establish a separation between the quasi-Fermi levels of the emitter (μ_h) , while the input heat (Q_h) is used to create a temperature difference and drive a net energy flux (E_{hc}) between the emitter and the cell. Output power (P_{out}) is generated at the cell by extracting current at μ_c , while waste heat (Q_c) is rejected to the environment. A portion of P_{out} is recycled back to the emitter, hence supplying P_{in} . The hot emitter also loses heat (Q_{loss}) to the environment (at 300 K) via far-field thermal radiation.

Figure 2. Spectral energy flux from a far-field, black body (BB) emitter (black), a near-field emitter (gray), and a near-field emitter with a small applied bias (red) at an emitter temperature of $T_h = 600$ K. The near-field enhancement factor ($f_{nf} = 5$), applied bias ($\mu_h = kT_h$), and bandgap ($E_g = 0.6$ eV) were chosen arbitrarily for illustration of the spectral energy flux.

Figure 3. Simulated efficiency as a function of transmission bandwidth for the following converters: (a) far-field, no parasitic heat losses ($\varepsilon_{sys} = 0$), (b) far-field, parasitic heat loss to the environment ($\varepsilon_{sys} = 0.05$), and (c) near-field ($f_{nf} = 50$), parasitic heat loss to the environment ($\varepsilon_{sys} = 0.05$). TPX with $E_{gl} = 1$ eV and $\mu_h = E_{gl} - 4kT_h$ (red), TPV_{leV} (black), and TPV_{4kT} (gray) are compared in each case. Carnot efficiency (dashed) is shown for reference. $T_h = 600$ K, $T_c = 300$ K.

Figure 4. Useful energy flux $(E_{hc}-P_{in})$ for far-field converters with heat loss to the environment $(\varepsilon_{sys}=0.05)$, corresponding to Fig. 3b. The following converters are compared: TPX with $E_{gl}=1$ eV and $\mu_h=E_{gl}-4kT_h$ (red), TPV_{leV} (black), and TPV_{4kT} (gray). Q_{loss} (dashed) is shown for reference.

Table 1. Converter parameters for the rigorous analysis of useful energy flux.

Figure 5. (a) Simulated energy-flux enhancement factor for $TPX_{1.424\text{eV}}$ relative to $TPV_{0.354\text{eV}}$ (red, solid) and $TPX_{0.75\text{eV}}$ relative to $TPV_{0.354\text{eV}}$ (black, solid) compared to the scaling relationship presented in Eq. 12 (dashed). (b) Above-bandgap spectral energy flux for $TPV_{0.354\text{eV}}$ (black), $TPX_{0.75\text{eV}}$ (gray), and $TPX_{1.424\text{eV}}$ (red). All converters have the same probability of occupying states above their respective bandgaps.

Figure 6. Simulated power enhancement factor for $TPX_{GaAs} - TPV_{InAs}$ (red, solid) and $TPX_{InGaAs} - TPV_{InAs}$ (black, solid) compared to the scaling relationship presented in Eq. 12 (dashed lines).

Figure 7. The spectral energy flux of (a) InAs and (b) InGaAs computed with MESH are compared to the spectral energy flux determined with the near-field approximation with near-field enhancement factors of 13 and 12.8 respectively.

Figure 8. Efficiency of TPX (red), TPV_{4kT} (gray), and TPV_{1eV} (red) under idealistic conditions (dashed) and with parasitic losses (solid).